Preliminary Evaluation of Drag Reduction Performance for Functional Surfaces with 60-degree Riblets Subjected to Taylor-Couette Flows

William B. Gordon[1,2], Evgueni V. Bordatchev[2,1], O. Remus Tutunea-Fatan[1,2], Naiheng Song[2], Lucy Li[2]
[1]Western University
1151 Richmond St, London, Canada
wgordon5@westerneng.ca; rtutunea@eng.uwo.ca
[2]National Research Council of Canada
800 Collip Circle, London, Canada
evgueni.bordatchev@nrc-cnrc.gc.ca; naiheng.song@nrc-cnrc.gc.ca; chun.li@nrc-cnrc.gc.ca

Abstract - This study outlines the initial development of a drag-reducing surface with a 60° triangular riblet-groove design. The research covers the design, microfabrication, and performance evaluation phases. The riblet-groove surface, designed with a lateral spacing of 57.8 µm and a depth of 50 µm, was based on optimized parameters from literature. Two acrylic drums were fabricated using high precision multi-axis single-point diamond turning technology, achieving excellent surface quality and form accuracy (< 2 µm). One drum had a flat surface, while the other featured the riblet-groove design. The functional performance was evaluated using a rheometer-based Taylor-Couette system, which recorded torque, angular position, and normal force synchronously and simultaneously in time domain. At high angular velocities, air naturally incorporated into the Taylor vortices, leading to an unexpected drag reduction of 39.7%, likely due to air bubbles trapped in the riblet valleys acting as a lubricant. Before air inclusion, the maximum drag reduction observed was 7.1%. Further research is needed to understand this significant improvement in drag reduction and explore its potential applications in aerospace, automotive, marine, energy, and biomedical industries.

Keywords: Turbulence, Rheometer, Taylor-Couette, Drag-Reduction, Functional Surfaces, Micro-Structures, Riblets

1. Introduction

Nature has long demonstrated the crucial role of drag forces in health, survival, and various applications, including military, performance, and efficiency [1]. The need to sense, control, and optimize drag forces—especially to reduce them—remains essential for advancing scientific understanding and engineering solutions in aerodynamics [2], hydrodynamics [3], and thermodynamics [4], particularly in aerospace, marine, automotive, biomedical, and wind energy sectors.

Drag force acts as a dynamic link between propulsion (e.g., airflow) and the system's response (e.g., wing deformations). In aerodynamics, two types of drag forces are involved: pressure-induced resistance and surface-induced drag, with the latter significantly dominating in aerodynamically shaped bodies [1]. Surface-induced drag, primarily due to friction at the flow-surface interface, causes turbulence and complex fluctuations in physical parameters, leading to increased skin resistance and energy dissipation through viscous friction.

Three main challenges exist in developing drag reduction technologies: i) designing, modeling, and simulating flow-surface dynamics to predict drag-reducing topographies [2, 5]; ii) advanced microfabrication of micro- and nano-scale geometric features with high surface quality and precision [6-8]; and iii) realistic performance evaluation of prototypes using conventional testing methods like wind tunnels, Taylor-Couette systems, and actual flight tests [9-14].

While microstructures have been known to reduce aerodynamic and hydrodynamic drag since the 1980s, only recent computational advancements have allowed for a deeper exploration of these effects. Studies on triangular and trapezoidal riblets have shown potential for environmental benefits and reduced fuel consumption in various aircraft [12-14]. However, their modest drag reduction (around 10%) and high implementation costs limit widespread adoption in military and commercial applications [15].

Extensive research has focused on the turbulent flow within the boundary layers of riblet microstructures. For instance, studies by Ancrum and Yaras [16] examined hairpin vortices generated by triangular riblets, and other research has shown drag-reducing properties in fish scale-inspired riblets by delaying turbulence [17, 18]. Direct Numerical Simulation (DNS)

has revealed that drag reduction is linked to the virtual origins of velocity components in turbulent flows over hydrophobic surfaces, although this effect diminishes with the onset of Kelvin-Helmholtz instabilities as riblets grow in size [19].

This study involved microfabricating two acrylic drums with design parameters previously used for numerical simulation using multi-axis single-point diamond turning technology. The performance of these drums was evaluated using a rheometer-based Taylor-Couette system, focusing on key flow dynamics such as torque, angular velocity, and drag reduction as a function of S^+ value. The dimensionless lateral spacing between riblets, denoted as S^+ *Eq. (1)*, is critical for drag reduction, with each type of riblet having an optimal S^+ value that can reduce skin friction by up to 5-10% when fully submerged in a homogeneous fluid [20]. When air is included in a fluid passing over a surface with riblets, air bubbles can get trapped inside the riblet valley and act as a lubricant for the faster moving fluid beyond the riblets causing the surface to act superhydrophobic [21, 22]. When conducting this study, it was found that air was included in the Taylor vortices at high angular velocities and produced higher than expected drag reduction compared with a homogeneous fluid test. The dimensionless lateral spacing between riblets is fundamentally defined as:

$$S^+ = su_\tau/\nu \text{ with } u_\tau = \sqrt{\tau_o/\rho}, \tag{1}$$

where s is the period of riblets (tip-to-tip distance), u_τ is the friction velocity of the smooth surface, ν is the kinematic viscosity of the fluid, τ_0 is the wall shear, and ρ is the density.

2. Design and Microfabrication

In this study, proven guidelines [2, 13, 20] were followed to create a functional surface with triangular riblets, having a tip-to-tip distance of 57.8 μm, riblet height of 50 μm, and an included angle of 60° (Fig. 1). This surface was applied to a drum with a 21.5 mm radius and 62.9 mm length for Taylor-Couette flow, similar to studies [11, 23, 24]. The experiment involved two coaxial cylinders: the outer hollow cylinder was fixed and functioned as a container, and the solid inner cylinder (drum with riblets) rotated with angular velocity ω. The outer cylinder had a radius of 25.0 mm, resulting in a radial gap of the physical domain $d = 3.5$ mm calculated as:

$$d = r_o - r_i \tag{2}$$

where r_o is the radius of the outer container and r_i is the radius of the drum, giving a gap ratio of $\eta = 0.86$ from $\eta = r_i/r_o$ and an axial aspect ratio of $\Gamma = \ell/d = 17.9$, where ℓ is the length (height) of the drum.

Two drums were fabricated according to these dimensions: one with a flat surface and the other with 60° riblets. Photographs of the drums are shown in Fig. 1. The optical image in Fig. 2a shows the riblets with no deformation, good straightness and surface quality (visible under a certain angle), and minimal burr formation (~2–3 μm). 3D surface topography measurements confirmed the surface quality and form accuracy, with riblet height and lateral spacing accurate to within 2 μm (Figs. 2b and 2c).
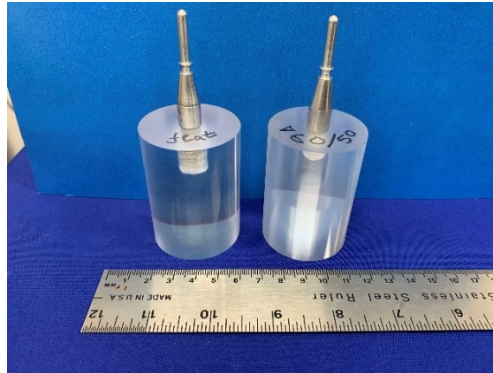

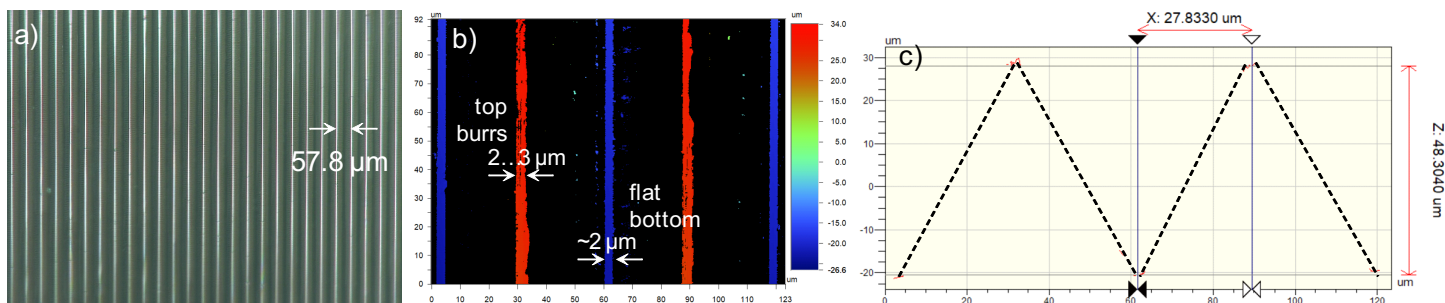Fig. 1: Microfabricated drums: with flat surface (left) and with 60° riblets (right).

Fig. 2: Results of microfabrication of 60° riblets: a) top view, b) surface topography, and c) surface profile.

3. Taylor-Couette Experimental Setup

The functional performance of microfabricated drums with 60° riblets was evaluated using a Kinexus Pro+ rheometer (Malven Instruments Ltd.) for Taylor-Couette flow measurements (Fig. 3). The rheometer's main component is a high-precision spindle mounted on air bearings, capable of rotating at angular velocities from 10 nrad·s⁻¹ to 500 rad·s⁻¹. It includes three key sensors for real-time measurements: i) applied torque (10 nN·m to 200 mN·m with a resolution 0.1 nN·m), ii) angular position (resolution <10 nrad), and iii) normal force (0.001 N to 20 N with a resolution 0.5 mN). The rheometer operates in shear rate and stress control modes. The inner drum with riblets, made from acrylic, was attached to the spindle via an M8x1 thread shaft, while the transparent acrylic outer container was mounted on the rheometer base and aligned with the drum and spindle. All dimensions of the components are provided in Section 2. The rSpace software (Malven Instruments Ltd.) was used to control the rheometer and record data on-line and synchronously with a sampling period of 1000 Hz.
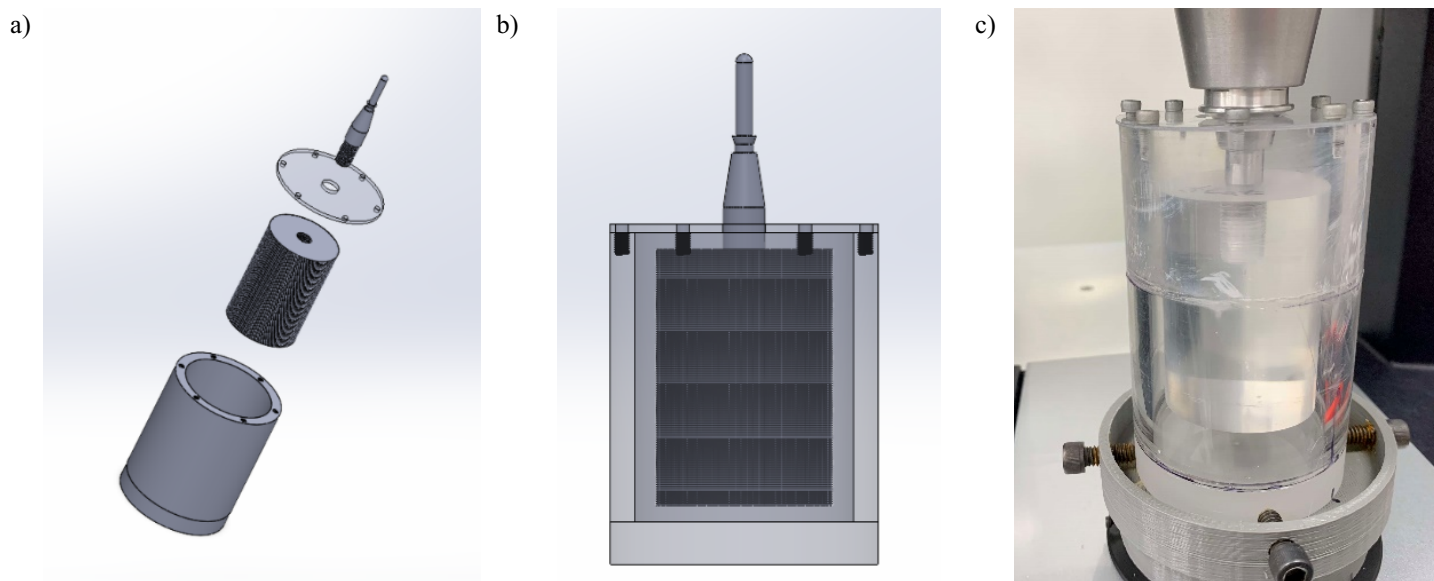

Fig. 3: Rheometer-based Taylor-Couette set-up for functional performance evaluation: a) components of the design, b) design assembly, and c) functional assembly.

4. Functional Performance Evaluation using Taylor-Couette set-up

The sequence used for these experiments spins the drum from $\omega = 8.28$ rad/s to 264.8 rad/s until the measured torque reaches a steady state value for 10 s. Multiple tests (at least 3) were run at each angular velocity for both the flat and 60° geometries (see Figs. 4a and 4b). It should be noted that the mass of each drum was normalized. Once entering the region with air incorporated into the Taylor vortices, the drum performance with flat geometry becomes more unstable than the 60° geometry. Additionally, the drag exhibited by the drum with flat geometry rises significantly. On the other hand, the drum with 60° geometry experiences a linear increase in torque in this secondary (unstable) region. This sudden increase in torque experienced by the flat drum and not the 60° drum causes a drastic decrease in the change in drag. It should be noted that a drag reduction of this magnitude, reaching a maximum of 40% (see Fig. 4c), is not typical of drag reducing micro-surfaces.

Interestingly, a possible reason for this difference between the results of this study and those found in the literature is the mixing of air into the Taylor vortices. It has been noted previously by [21, 22] that inclusion of air bubbles in the riblet valleys can drastically improve the drag reduction relative to a situation without air. Prior to the inclusion of air into the Taylor vortices a drag reduction of 4.5-7.1% was found for $S^+ = 2.5$-10.
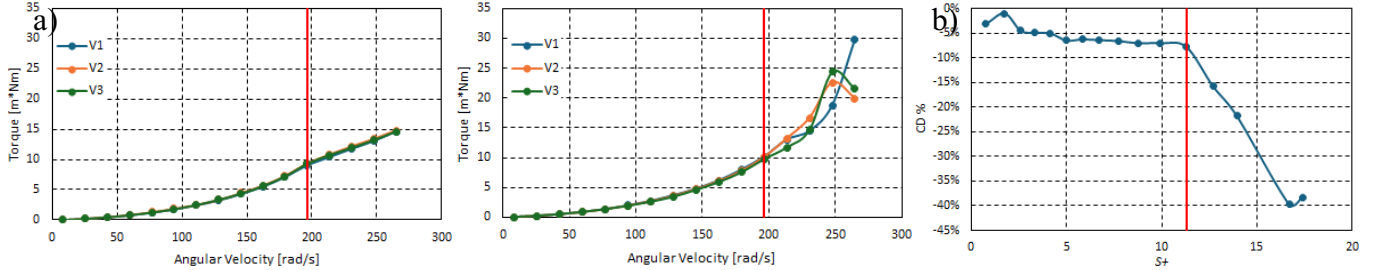

Fig. 4: Results of functional performance evaluation by comparing drums with flat surface and with 60° riblets: a) 60° drum: torque *vs.* angular velocity, 3 trials, b) flat drum: torque *vs.* angular velocity, 3 trials, and c) change in drag *vs.* S^+ value. The red vertical line in all of the plots represents the transition between having no bubbles and having air inside the Taylor vortices.

Furthermore, analysis of the transient torque and angular velocity readings from the rheometer was conducted to gain deeper understanding of the functional performance. Figs. 5-8 show the analysis of the 60° riblets and the flat surface at two different angular velocities 59.6 rad/s and 247.7 rad/s. The measured torque $T(t)$ can be represented as a linear combination of three components: i) mean value, ii) periodic (quasi-dynamic) component, iii) and dynamic component as

$$T(t) = T_o + \tilde{T}(t) + \hat{T}(t) \text{ with } \tilde{T}(t) = A \sin(\omega t) \tag{3}$$

where $T(t)$ is the measured torque signal, T_o is the mean torque, $\tilde{T}(t) = A \sin(\omega t)$ is the periodic component with the amplitude A and the angular velocity ω corresponded to the rotational deviations, and $\hat{T}(t)$ is the dynamic component induced by the hydrodynamic phenomena (including drag) at surface-liquid interface.

The mean torque is used to find the data points in Figs. 4a and 4b after averaging the original toque over a course of 10 s once reaching a steady state condition after changing the rotational speed. Figs. 5a and 6a show the original torque measurements at $\omega = 59.6$ rad/s for the 60° and flat sample, respectively, while Figs. 7a and 8a are at $\omega = 230.6$ rad/s. The periodic component is caused by slight misalignments of the rheometer shaft, drum, and imperfections in the manufacturing processes of the drums and shafts and are shown in Figs. 5b-8b. The dynamic component is caused by the interface of the surface and the turbulent fluid flow and is shown in Fig. 5e-8e. Parameters (mean and standard deviation (STD)) of original data $T(t)$ and periodic $\tilde{T}(t)$ and dynamic $\hat{T}(t)$ components as well as dominant frequency and its amplitude of Fast Fourier Transform (FFT) amplitude-frequency characteristic (AFC) of $\tilde{T}(t)$ (see Figs. 5c-8c) are presented in Table 1.

Table 1: Parameters of original data $T(t)$ and periodic $\tilde{T}(t)$ and dynamic $\hat{T}(t)$ components.

rotational speed, rad/s	original data $T(t)$				periodic $\tilde{T}(t)$		dynamic $\hat{T}(t)$
	mean	STD	AFC frequency	AFC amplitude	magnitude	STD	STD
	mN·m	mN·m	Hz	mN·m/Hz	mN·m	mN·m	mN·m
59.6 (flat drum)	0.91	0.087	9.5	0.105	0.26	0.085	0.017
59.6 (60° drum)	0.88	0.080	9.5	0.105	0.24	0.078	0.018
230.6 (flat drum)	12.83	1.011	36.7	0.997	2.45	0.817	0.591
230.6 (60° drum)	12.25	1.000	36.7	1.293	2.69	0.912	0.398

The original torque measurements $T(t)$ at $\omega = 59.6$ rad/s and at $\omega = 230.6$ rad/s always demonstrate that the mean and STD values are always lower for the 60° drum than for the flat drum, e.i., 0.88 mN·m *vs.* 0.91 mN·m and 0.080 mN·m *vs.* 0.087 mN·m at $\omega = 59.6$ rad/s, respectively, and 12.25 mN·m *vs.* 12.83 mN·m and 1.00 mN·m *vs.* 1.011 mN·m at $\omega = 230.6$ rad/s, respectively. These parameters are quantitively estimates the torque and therefore drag decrease for both rotational speeds. This trend continuous for the analysis of periodical components $\tilde{T}(t)$ whereas magnitude value decreases

from 0.26 mN·m (flat drum) to 0.24 mN·m (60° drum) and STD value decreases from 0.085 mN·m (flat drum) to 0.078 mN·m (60° drum) at ω = 59.6 rad/s. However, functional performance at ω = 230.6 rad/s shows opposite situation, when magnitude and STD values for 60° drum are higher than for the flat drum. This due to non-stationary behavior of Taylor vortices (see Table 1).
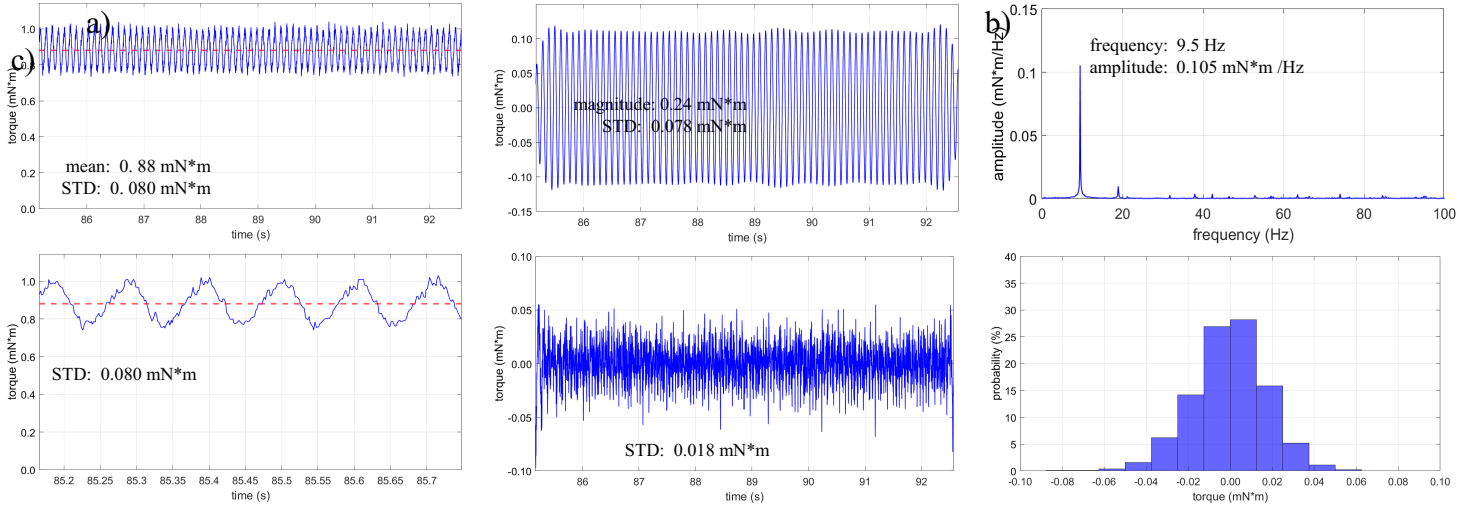

Fig. 5: 60° drum performance at 59.6 rad/s: a) original torque data, b) kinematic component, c) FFT AFC of original torque data, (d) zoomed-in kinematic component, e) dynamic component, and f) histogram of the original torque data.
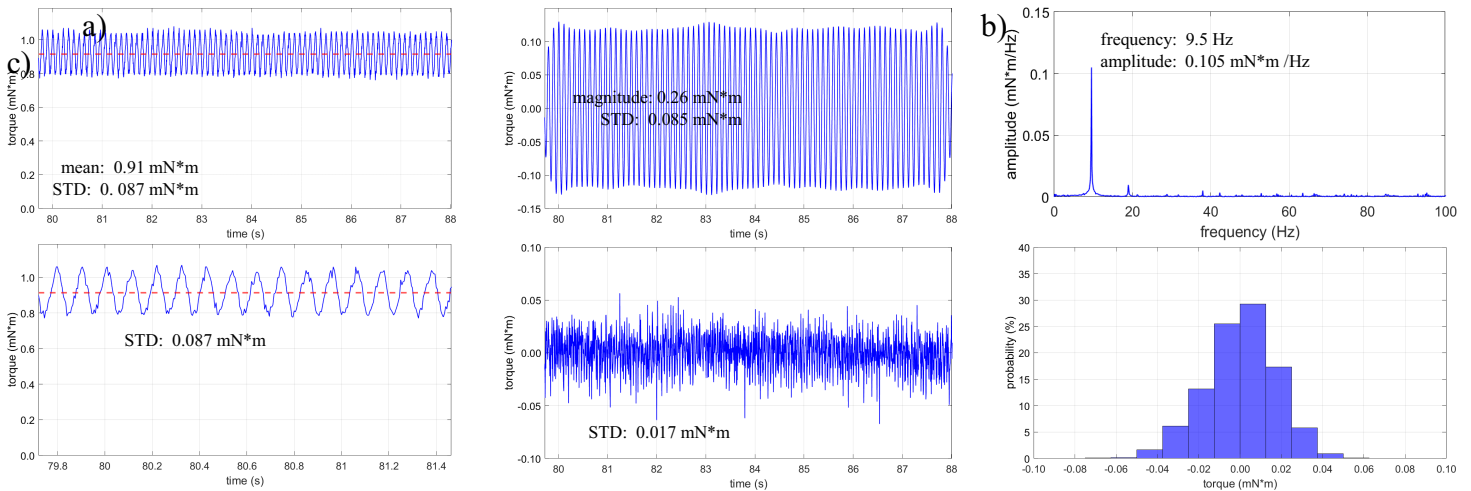

Fig. 6: Flat drum performance at 59.6 rad/s: a) original torque data, b) kinematic component, c) FFT AFC of original torque data, (d) zoomed-in kinematic component, e) dynamic component, and f) histogram of the original torque data.
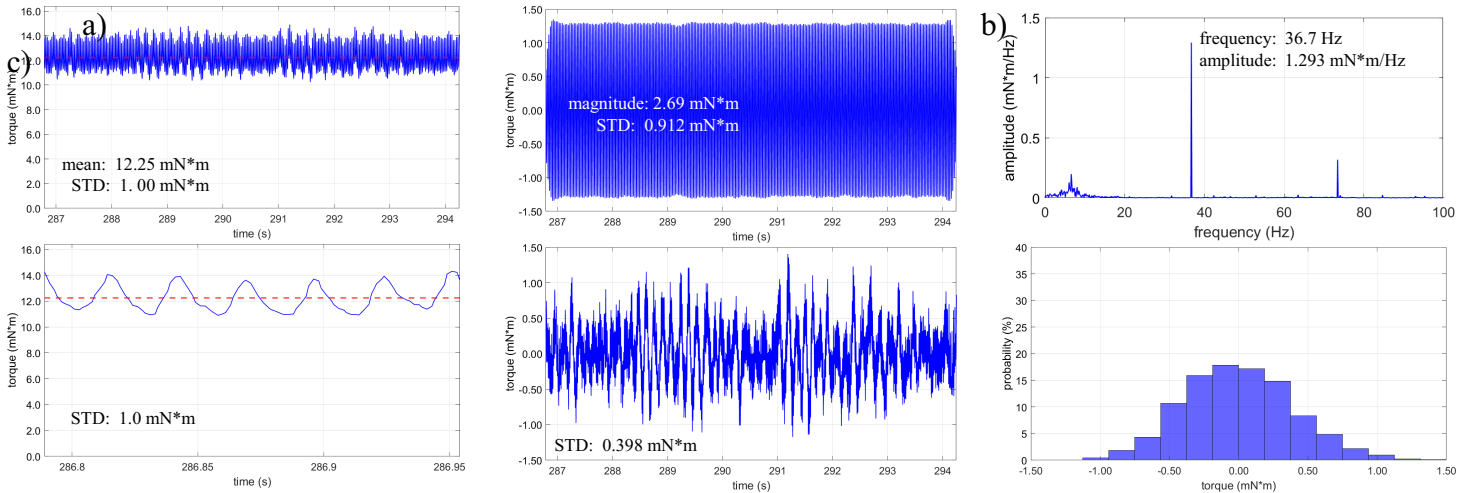
Fig. 7: 60° drum performance at 230.6 rad/s: a) original torque data, b) kinematic component, c) FFT AFC of original torque data, (d) zoomed-in kinematic component, e) dynamic component, and f) histogram of the original torque data.
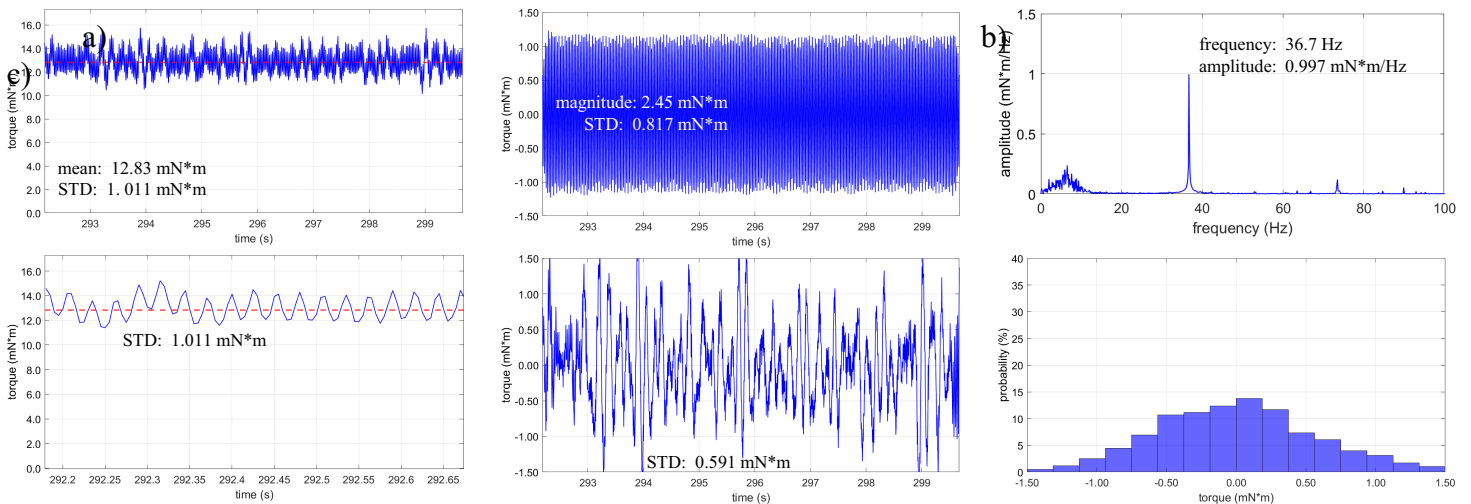

Fig. 8: Flat drum performance at 230.6 Rad/s: a) original torque data, b) kinematic component, c) FFT AFC of original torque data, (d) zoomed-in kinematic component, e) dynamic component, and f) histogram of the original torque data.

Additionally, at ω = 230.6 rad/s the 60° drum had a slightly higher STD of the dynamic component, see Fig. 7e and 8e. Interestingly, this trend is swapped for the kinematic component of the signal, where at ω = 59.6 rad/s the 60° drum had a slightly higher STD and at ω = 230.6 rad/s it was lower than the flat sample, see Figs. 5b-8b. As expected, the case with the higher angular velocity has significantly more dynamic interactions, interestingly, this component is mostly at a lower frequency than the periodic component of the signal. Furthermore, observing the FFTs of the signals in Fig. 5c-8c shows that the flat surface has slightly more low frequency signals when bubbles are included compared to the 60° sample. Histograms of $T(t)$ (see Figs. 5f-8f) show that at ω = 230.6 Rad/s the torque amplitudes are more spread out compared with the ω = 59.6 rad/s experiments. Future studies could compare these dynamic components to the total kinetic energy (TKE) observed either in computational fluid dynamics (CFD) simulations or particle image velocimetry (PIV) experiments which is dependent on the root-mean-square (RMS) velocity fluctuations. This interaction between the surface, air and water interfaces is not clearly understood yet and will require more efforts to visualize and quantify the phenomena.

5. Conclusions

This work presents the preliminary development of a drag-reducing surface with a 60° triangular riblet-groove design, covering its design, microfabrication, and performance evaluation. The riblet-groove surface featured a lateral spacing of 57.8 µm and a depth of 50 µm, optimized from literature. Two acrylic drums were microfabricated using multi-axis single-point diamond turning technology with high surface quality and form accuracy (< 2 µm): one with a flat surface and the other with the riblet-groove surface. Performance evaluation was conducted using a rheometer-based Taylor-Couette measuring system, synchronously recording torque, position, and force. Three performance characteristics were calculated: torque vs. angular velocity, drag reduction *vs.* S^+ value, and the signal components of the measured torque *vs.* time. A drag reduction of 4.5-7.1% was achieved before air bubble inclusion, with a maximum drag reduction of 39.7% at $S^+ = 16.7$ after air was incorporated into the Taylor vortices at $S^+ = 11.3$. The flat surface exhibited significantly higher low-frequency noise levels after air inclusion. Future studies could improve the air trap on the rheometer to prevent air from being included in the moving water, increase the riblet spacing of the drums to shift the S^+ values higher without increasing angular velocity, and compare the dynamic component measured by the rheometer to TKE analysis in PIV experiments or CFD simulations.

Acknowledgments

References

[1] Abdulbari, H. A., Mahammed, H.D., and Hassan, Z.B.Y., "Bio-inspired passive drag reduction techniques: A review," *ChemBioEng Reviews*, Vol. 2, No.3, 2015, pp. 185–203.
doi: 10.1002/cben.201400033

[2] Pakatchian, M.R., Rocha, J., and Li, L., "Advances in Riblets Design," *Applied Sci*ence, Vol. 13, paper 10893, 2023, 36 pp.
doi: 10.3390/app131910893

[3] Abdulbari, H.A., Yunus, R.M., Abdurahman, N.H., and Charles, A., "Going against the flow—A review of non-additive means of drag reduction," *Journal of Industrial and Engineering Chemistry*, Vol. 19, 2013, pp. 27–36.
doi: 10.1016/j.jiec.2012.07.023

[4] Thompson, E. J. B. and Gunasekaran, M., "Review analysis on riblets used in thermal applications and wind turbines," *Journal of Thermal Analysis and Calorimetry*, 2023
doi: 10.1007/s10973-023-12494-6

[5] Mele, B., "Riblet drag reduction modeling and simulation," *Fluids*, Vol. 7, No. 7, paper 249, 2022, 15 pp.
doi: 10.3390/fluids7070249

[6] Brinksmeier, E., Gläbe, R., and Schönemann, L., "Review on diamond-machining processes for the generation of functional surface structures," *CIRP Journal of Manufacturing Science and Technology*, Vol. 5, 2012, pp. 1–7.
doi: 10.1016/j.cirpj.2011.10.003

[7] Coblas, D. G., Fatu, A., Maoui, A., and Hajjam, M., "Manufacturing textured surfaces: state of art and recent developments," *Proceedings of the Institution of Mechanical Engineers, Part J: Journal of Engineering Tribology*, Vol. 229, 2014, pp. 3–29.
doi: 10.1177/1350650114542242

[8] Bordatchev, E.V. Tauhiduzzaman, M., Kugler, T., Katz, A., and Bohr, R., "Demonstration of advanced capabilities of 5-axis micromilling: geometries with high-aspect ratio and/or optical surface quality," *Proceeding of the 8th International Conference on Micro Manufacturing*, Victoria, BC, Canada, 2013, pp. 357–362.
doi: n/a

[9] Chamorro, L., Arndt, R., and Sotiropoulos, F., "On the skin friction drag reduction in large wind turbines using sharp V-grooved riblets," *Proceeding of the 49th AIAA Aerospace Sciences Meeting*, 2011, paper AIAA 2011-351, 7 pp.
doi: 10.2514/6.2011-351

[10] Hamilton, B.W., Tutunea-Fatan, O.R., and Bordatchev, E.V., "Drag reduction by fish-scale inspired transverse asymmetric triangular riblets: Modelling, preliminary experimental analysis and potential for fouling control," Biomimetics, Vol. 8, No. 3, paper 324, 2023, 15 pp.
doi:

[11] Leitl, P.A., Kuntzagk, S., Flanschger, A., and Pfingsten, K., "Experimental and numerical investigation of the reduction in skin friction due to riblets applied on the surface of a Taylor-Couette cell," AIAA Scitech 2019 Forum, 19 pp.
doi: 10.2514/6.2019-1625

[12] Leitl, P. A., Smoker, J., Garcia de Albeniz, M. L., and Flanschger, A., "Numerical and experimental investigation of different Riblet layouts on a Stratos 716 x business jet," *AIAA SCITECH 2023 Forum*, 15 pp.
doi: 10.2514/6.2023-1952

[13] Viswanath, P.R., "Aircraft viscous drag reduction using riblets," *Progress in Aerospace Sciences*, Vol. 38, No. 6–7, 2002, pp. 571–600.
doi: 10.1016/s0376-0421(02)00048-9

[14] Cacciatori, L., Brignoli, C., Mele, B., Gattere, F., Monti, C., and Quadrio, M., "Drag reduction by riblets on a commercial UAV," *Applied Sciences*, Vol. 12, No. 10, paper 5070, 17 pp., 2022.
doi: 10.3390/app12105070

[15] Smith, B. R., Yagle, P., and McClure, P. D., "Computational simulation of staggered 3-D riblets for skin friction drag reduction," *AIAA SCITECH 2023 Forum*, 2023, 12 pp.
doi: 10.2514/6.2023-1763

[16] Ancrum, D.B. and Yaras, M.I., "Measurements of the effects of streamwise riblets on boundary layer turbulence," *Journal of Fluids Engineering*, Vol. 139, No. 11, paper 111203, 2017, 10 pp.
doi: 10.1115/1.4037044

[17] Muthuramalingam, M., Villemin, L.S., and Bruecker, C., "Streak formation in flow over biomimetic fish scale arrays," *Journal of Experimental Biology*, Vol. 222, paper jeb205963, 2019, 11 pp.
doi: 10.1242/jeb.205963

[18] Muthuramalingam, M., Puckert, D.K., Rist, U., and Bruecker, C., "Transition delay using biomimetic fish scale arrays," *Scientific Reports*, Vol. 10, No. 1, paper 14534, 2020, 13 pp.
doi: 10.1038/s41598-020-71434-8

[19] Gómez-de-Segura, G., Sharma, A., and García-Mayoral, R., "Turbulent drag reduction using anisotropic permeable substrates," *Flow, Turbulence and Combustion*, Vol. 100, No. 4, 2018, pp. 995–1014.
doi: 10.1007/s10494-018-9916-4

[20] Bechert, D.W., Bruse, M., and Hage, W., van der Hoeven, J.G.T., and Hoppe, G., "Experiments on drag-reducing surfaces and their optimization with adjustable geometry", *Journal of Fluid Mechanics*, Vol. 338, 1997, pp. 59–87.
doi: 10.1017/s0022112096004673

[21] R. García-Mayoral, G. Gómez-de-Segura, and C. T. Fairhall (2019). "The control of near-wall turbulence through surface texturing." Fluid Dynamics Research 51(1).

[22] G. M. DI CICCA, G. IUSO, P. G. SPAZZINI, and M. ONORATO, "Particle image velocimetry investigation of a turbulent boundary layer manipulated by Spanwise Wall Oscillations," Journal of Fluid Mechanics, vol. 467, pp. 41–56, Sep. 2002. doi:10.1017/s002211200200157x

[23] Greidanus, A. J., Delfos, R., Tokgoz, S., and Westerweel, J., "Turbulent Taylor–Couette flow over riblets: drag reduction and the effect of bulk fluid rotation," *Experiments in Fluids*, Vol. 56, No. 5, paper 107, 2015, 13 pp.
doi: 10.1007/s00348-015-1978-7

[24] Xu, B., Li, H., Liu, X., Xiang, Y., Lv, P., Tan, X., Zhao, Y., Sun, C., and Duan, H., "Effect of micro-grooves on drag reduction in Taylor–Couette flow," *Physics of Fluids*, Vol. 35, paper 043608, 2023, 10 pp.
doi: 10.1063/5.0145900